Pyrochlore-Type Iron Hydroxy Fluorides as Low-Cost Lithium-Ion Cathode Materials for Stationary Energy Storage

Julian Felix Baumgärtner, Michael Wörle, Christoph P. Guntlin, Frank Krumeich, Sebastian Siegrist, Valentina Vogt, Dragos C. Stoian, Dmitry Chernyshov, Wouter van Beek, Kostiantyn V. Kravchyk,* and Maksym V. Kovalenko*

Pyrochlore-type iron (III) hydroxy fluorides (Pyr-IHF) are appealing low-cost stationary energy storage materials due to the virtually unlimited supply of their constituent elements, their high energy densities, and fast Li-ion diffusion. However, the prohibitively high costs of synthesis and cathode architecture currently prevent their commercial use in low-cost Li-ion batteries. Herein, a facile and cost-effective dissolution–precipitation synthesis of Pyr-IHF from soluble iron (III) fluoride precursors is presented. High capacity retention by synthesized Pyr-IHF of >80% after 600 cycles at a high current density of 1 A g^{-1} is obtained, without elaborate electrode engineering. Operando synchrotron X-ray diffraction guides the selective synthesis of Pyr-IHF such that different water contents can be tested for their effect on the rate capability. Li-ion diffusion is found to occur in the 3D hexagonal channels of Pyr-IHF, formed by corner-sharing FeF$_{6-x}$(OH)$_x$ octahedra.

1. Introduction

The shift from fossil fuels to CO_2-emission-free renewables such as solar and wind is impeded substantially by the absence of inexpensive stationary rechargeable batteries, which are required for stabilizing the energy production–consumption misbalance because of the intermittent characteristic of renewable energy sources.[1,2] The capital cost of these stationary batteries has higher importance than their energy density and can be satisfied only when a battery is composed entirely of low-cost, earth-abundant, and convenient-to-produce constituents.[3–6] To achieve this goal, iron (III) fluoride-based compounds are being intensely explored as inexpensive cathode active materials for lithium-ion batteries (LIBs).[7–13] They possess numerous advantages such as an abundance of constituent chemical elements, high lithiation potentials of 2.7–3.1 V versus Li$^+$/Li, and a high theoretical capacity of 237 mA h g^{-1} for one-electron operation. Iron (III) fluorides with a pyrochlore-type structure (Pyr-FeF$_3$) are of particular interest owing to the presence of large hexagonal channels formed from corner-sharing FeF$_6$ octahedra.[12,14,15] This structural feature is expected to facilitate Li-ion diffusion and consequently should lead to improved rate capability and decreased voltage hysteresis as compared to ReO$_3$-type iron (III) fluorides (r-FeF3), which exhibit narrower Li-ion diffusion channels (**Figure 1**a).[16] Although structurally related tetragonal FeF$_3$(H$_2$O)$_2$ · H$_2$O and hexagonal-tungsten-bronze-type FeF$_3$ · 0.33 H$_2$O also comprise channels inside the structure (Figure 1a),[17,18] they extend in only 1D and therefore may be blocked upon amorphization (loss of long-range order) caused by prolonged cycling.[19] By comparison, the interconnected channels along (110) and equivalent directions in Pyr-FeF$_3$ (3D) might retain some connectivity and therefore Li-ion diffusion paths, even upon amorphization.[14]

Despite the great potential of Pyr-FeF$_3$ as a low-cost cathode active material, no cost-effective and robust synthesis of Pyr-FeF$_3$ has been developed yet. Pyr-FeF$_3$ was first synthesized by De Pape et al. in 1986 by a high-temperature solid-state reaction of FeF$_2$ and FeF$_3$ with the hazardous and highly toxic NH$_4$F, followed by oxidizing the NH$_4$Fe$_2$F$_6$ product in a boiling Br$_2$ solution and high-vacuum treatment.[20] In 2010–2013, Li et al. reported an alternative approach by dissolving Fe(NO$_3$)$_3$ · 9H$_2$O in rather expensive tetrafluoroborate ionic liquids which acted both as templating agents and fluorine sources. Heating the solution yielded the Pyr-FeF$_3$ · 0.5 H$_2$O precipitate.[14,21] Most

J. F. Baumgärtner, M. Wörle, C. P. Guntlin, F. Krumeich, S. Siegrist, V. Vogt, K. V. Kravchyk, M. V. Kovalenko
Laboratory of Inorganic Chemistry
Department of Chemistry and Applied Biosciences
ETH Zürich
Zürich CH-8093, Switzerland
E-mail: kostiantyn.kravchyk@empa.ch; mvkovalenko@ethz.ch
J. F. Baumgärtner, K. V. Kravchyk, M. V. Kovalenko
Laboratory for Thin Films and Photovoltaics
Empa – Swiss Federal Laboratories for Materials Science & Technology
Dübendorf CH-8600, Switzerland
D. C. Stoian, D. Chernyshov, W. van Beek
Swiss–Norwegian BeamLines at the European Synchrotron Radiation Facility
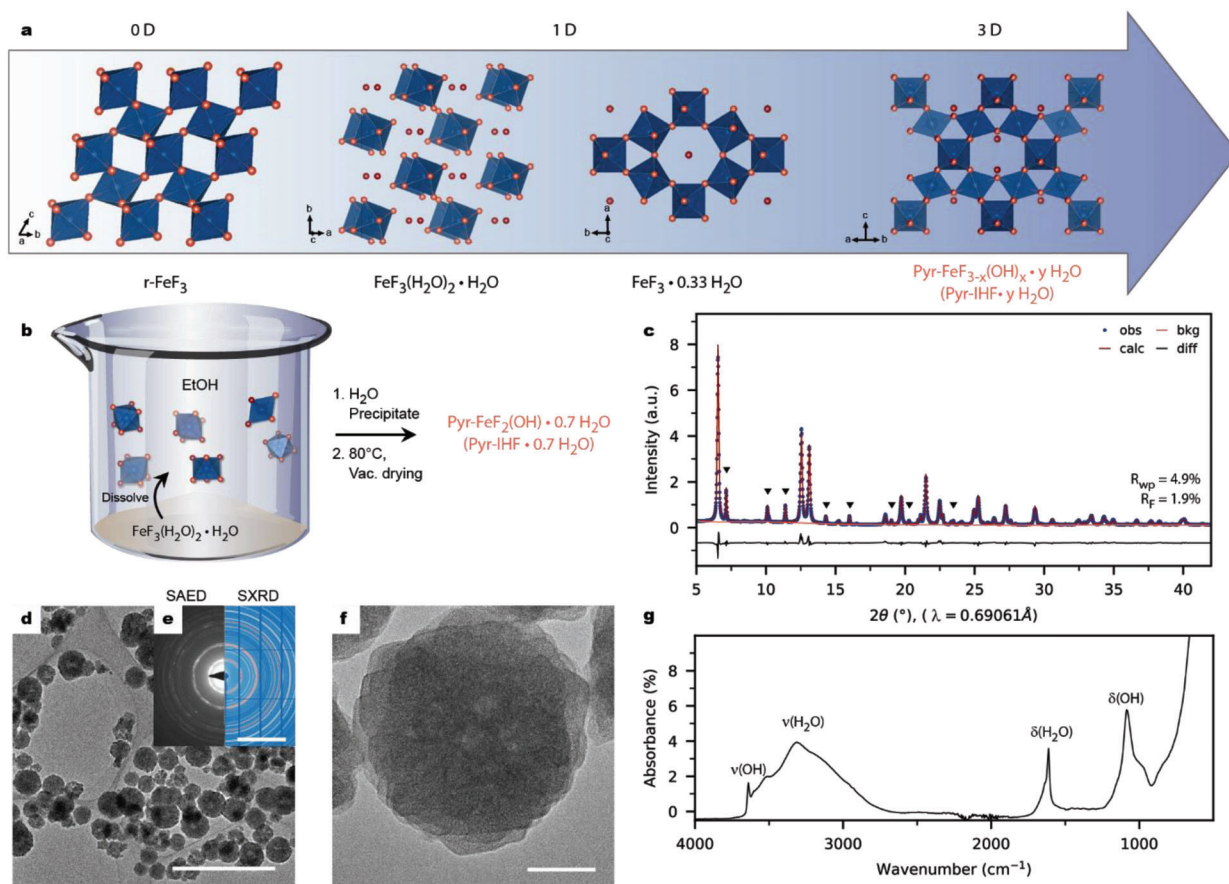Grenoble 38000, France

Figure 1. Synthesis and Characterization of Pyrochlore Iron Hydroxy Fluoride (Pyr-IHF). a) Schematic overview of different iron fluoride crystal structures and the dimensionality of their channels. b) Schematic representation of the synthesis. $FeF_3(H_2O)_2 \cdot H_2O$ dissolves in EtOH and the dissolved solution is centrifuged away while the remaining precipitate can be reused for further syntheses. Pyr-IHF precipitates from the ethanolic solution upon the addition of H_2O and is isolated by centrifuging and drying. c) Rietveld refinement using the synchrotron powder diffraction patterns of as-synthesized Pyr-IHF (triangles indicate $FeF_3(H_2O)_2 \cdot H_2O$ impurities). d,f) TEM micrographs of as-synthesized Pyr-IHF at different magnifications (scale bars 1 µm for (d) and 50 nm for (f)). e) Comparison of the SAED and SXRD pattern for as-synthesized Pyr-IHF (scale bar 5 nm^{-1}). g) Fourier-transform infrared spectrum of as-synthesized Pyr-IHF, proving the presence of hydroxide ligands around Fe. ν(XY) and δ(XY) represent stretching modes and bending modes, respectively.

recently, a hydrothermal synthesis employing $FeCl_2 \cdot 4 H_2O$ and HF, followed by heat treatment, was reported by Lemoine et al.[15] Inspired by the synthesis of porous materials, such as metal–organic frameworks,[22] zeolites,[23] and Prussian blue analogs,[24] which often employ dissolved precursor building blocks that condense into the desired porous structure in the presence of a suitable templating agent, we reasoned that a similar approach could be used to synthesize the pyrochlore-type structure at ambient conditions (Figure 1b).

Here, we report the synthesis of pyrochlore-type iron hydroxy fluoride (Pyr-IHF) under ambient conditions from $FeF_3(H_2O)_2 \cdot H_2O$ precursor dissolved in ethanol. The synthesis is performed by injecting a small quantity of water into the ethanolic solution of dissolved $FeF_3(H_2O)_2 \cdot H_2O$ precursor, thus triggering the precipitation of Pyr-IHF. The subsequent heat-treatment of the as-synthesized Pyr-IHF allows the selective removal of the templating molecules of water from the 3D channels, as proven by operando synchrotron XRD (SXRD) combined with thermogravimetric analysis and mass spectrometry (TGA-MS). The Pyr-IHF cathodes exhibited superior cycling stability

of >80% capacity retention after 600 cycles at high current rates (1 A g^{-1}), on par with state-of-the-art iron fluoride cathodes but without the need for nanostructuring or tailored architectures normally required for iron (III) (hydroxy) fluoride-containing cathodes. Motivated by the idea that selective removal of H_2O from the channels of the pyrochlore structure could enhance Li-ion diffusion and thereby the rate capability, we also performed a series of electrochemical measurements on Pyr-IHF cathodes with different water content. Our results clearly show the deteriorating effect of H_2O inside the channels on the capacity, and thereby demonstrate, for the first time, that Li-ions diffuse along the 3D channels of the pyrochlore structure.

2. Results and Discussion

2.1. Synthesis and Characterization of Pyrochlore Iron Hydroxy Fluoride

In short, Pyr-IHF was synthesized as follows (Figure 1b; Figure S1, Supporting Information). $FeF_3(H_2O)_2 \cdot H_2O$ (1.00 g) was

**ADVANCED
SCIENCE NEWS**

www.advancedsciencenews.com

**ADVANCED
MATERIALS**

www.advmat.de

partially dissolved in 150 mL of ethanol (EtOH) at room temperature (RT) by stirring for ≈6 h. The formed ethanolic solution (1.00 g_{Fe} L_{EtOH}^{-1}) was separated from the undissolved $FeF_3(H_2O)_2 \cdot H_2O$ by centrifugation and filtering. Subsequently, 6 ml of H_2O (4 vol.%) was injected into the ethanolic solution, resulting in the slow precipitation of beige-colored Pyr-IHF (0.176 g, ≈55% yield based on the dissolved precursor). The precipitate was dried under vacuum at ≈40 °C for at least 3 h for further use. The synthesis is described in detail in the Experimental Section. The cost-effectiveness of our synthesis is highlighted by the estimated raw material cost of ≈14 $ kg^{-1} for Pyr-IHF (Note S1, Supporting Information).

As-synthesized Pyr-IHF is composed of highly polycrystalline, 200 nm spherical nanoparticles with a narrow particle size distribution as indicated by scanning, transmission, and scanning-transmission electron microscopy (SEM, TEM, STEM) micrographs and the selected area electron diffraction (SAED) patterns (Figure 1d–f; Figures S2–S4, Supporting Information). The formation of a cubic pyrochlore structure (space group *Fd-3m* (227)[20] with 3D interconnected hexagonal channels was confirmed by SXRD measurements of the precipitate as shown in Figure 1c, with traces of $FeF_3(H_2O)_2 \cdot H_2O$ impurities.[17] Fe^{3+} ions are surrounded by six F^-/OH^- anions at the same 48f Wyckoff position (mixed occupancy). While F^- and OH^- ligands cannot be distinguished by powder XRD, the presence of OH^- was confirmed by the sharp band at 3640 cm^{-1} in the Fourier-transform infrared spectrum of the as-synthesized Pyr-IHF sample (Figure 1g). To quantify the amount of F^- and OH^- ligands in as-synthesized Pyr-IHF, we measured the extended X-ray absorption fine structure (EXAFS) spectra of samples with known O: F ratio and performed wavelet transforms on the acquired spectra (Figures S5,S6, Supporting Information).[25] By analyzing the wavelet intensity maxima in *k*-space and correlating them with the number of F^- ligands in the coordination environment of Fe^{3+}, we observed a linear dependence (R^2 = 0.992) (Figure S6e, Supporting Information). Subsequently, the number of F^- and OH^- ligands in the as-synthesized Pyr-IHF was determined by fitting the measured wavelet intensity maximum. The analysis revealed an average environment consisting of ≈4.3 F^- and 1.7 OH^- ligands around Fe^{3+} in the Pyr-IHF sample, which closely matches the average environment observed in the $FeF_3(H_2O)_2 \cdot H_2O$ precursor with 4 F^- and 2 O ligands around Fe^{3+}. We note that the local environment for individual $FeF_{6-x}(OH)_x$ octahedra might deviate from the average $FeF_4(OH)_2$ environment.

To determine the presence of water of crystallization within the channels of Pyr-IHF and the amount of $FeF_3(H_2O)_2 \cdot H_2O$ impurities, Rietveld refinement was performed using the structural parameters of Pyr-FeF_3 (a = 10.325(2) Å).[20] The presence of water of crystallization (0.7 H_2O per formula unit) was modeled with oxygen atoms at the Wyckoff position 8b (⅜, ⅜, ⅜) and partial occupancy at 16d (¾, ¾, ½) (Note S2, Figure S7, Table S1, Supporting Information). The addition of this water of crystallization significantly improved the model fit ($R_{F, with H2O}$ = 1.90% vs $R_{F, without H2O}$ = 5.24%). The presence of H_2O may also explain the significantly larger lattice parameter (a = 10.47760(16) Å) for Pyr-IHF compared to previously reported Pyr-FeF_3 (a = 10.325(2) Å).[20] This refined content of structural water, combined with the EXAFS analysis, suggests a sum formula of approximately $FeF_2(OH) \cdot 0.7$ H_2O for as-synthesized Pyr-IHF.

2.2. Structural and Morphological Changes During Heat-Treatment

For comprehending the chemical transformations that occur during heating of the as-synthesized Pyr-IHF powder, it was analyzed by operando SXRD upon heating to 280 °C followed by cooling, both at the same rate of 12 K min^{-1}. The lattice parameter contracts in two steps from 10.48 Å to 10.43 Å between 75 – 125 °C and then to 10.37 Å between 220 – 280 °C as indicated by the shifted SXRD reflection positions of Pyr-IHF to higher values (**Figure 2**a–d; Figure S8, Supporting Information). From additional TGA-MS performed on Pyr-IHF at the analogous heat-treatment rate used in the SXRD experiment (Figure 2g,h), it was determined that the first unit cell contraction is caused by the release of water molecules, as evidenced by the appearance of an H_2O MS peak starting at 75 °C. Since the occupancy of H_2O on the Wyckoff sites 8b and 16d as determined by sequential Rietveld refinement did not change between 75 – 125 °C (Figure 2e), it was concluded that the first unit cell contraction and appearance of an H_2O MS signal was associated with the release of surface adsorbed water and disordered water molecules within the channels rather than water of crystallization (see Note S3, Supporting Information for a more detailed TGA analysis). Simultaneously, at ≈75 °C, the disappearance of XRD reflections of $FeF_3(H_2O)_2 \cdot H_2O$ impurities was observed (Figure 2b; Figure S9, Supporting Information). This is consistent with previous observations that $FeF_3(H_2O)_2 \cdot H_2O$ amorphizes when heat-treated under air.[26] The second unit cell contraction within the temperature range of 220 – 280 °C is associated with the release of the water of crystallization, as confirmed by the decrease in O occupancy at the 8b site and the appearance of an additional peak in the H_2O MS signal. Moreover, a small CO_2 MS peak above 220 °C indicates the combustion of EtOH (Figures S10,S11, Supporting Information). Considering that EtOH is too large to fit into the 3D hexagonal channels of Pyr-IHF, formed by corner-sharing $FeF_4(OH)_2$ octahedra, the CO_2 MS signal is possibly caused by small amounts of EtOH trapped in nanopores that form during the rapid nucleation and precipitation of Pyr IHF.

Meanwhile, no HF signal was observed during any TGA-MS measurements, excluding the release of HF. Notably, when the heat treatment is performed in the air (i.e., in the presence of moisture), Pyr-IHF can be partially rehydrated upon cooling, as indicated by the increased O occupancy at the 8b site during cooling (Figure S9, Supporting Information).

It has previously been reported that hexa-tungsten-bronze-type iron hydroxy fluorides exhibit significant dehydroxylation of the hydroxide ligands during prolonged heating at 300 °C.[27] To test if dehydroxylation is also prominent during the operando SXRD experiment, we performed an additional Rietveld refinement of Pyr-IHF at 280 °C. Since dehydroxylation would create a stoichiometric number of vacancies, thereby reducing the occupancy on the Wyckoff position 48f, we varied the occupancy of the 48f site to test for dehydroxylation. The obtained occupancy at the 48f site was 101%, thereby excluding the possibility of significant dehydroxylation in Pyr-IHF during the heat treatment.
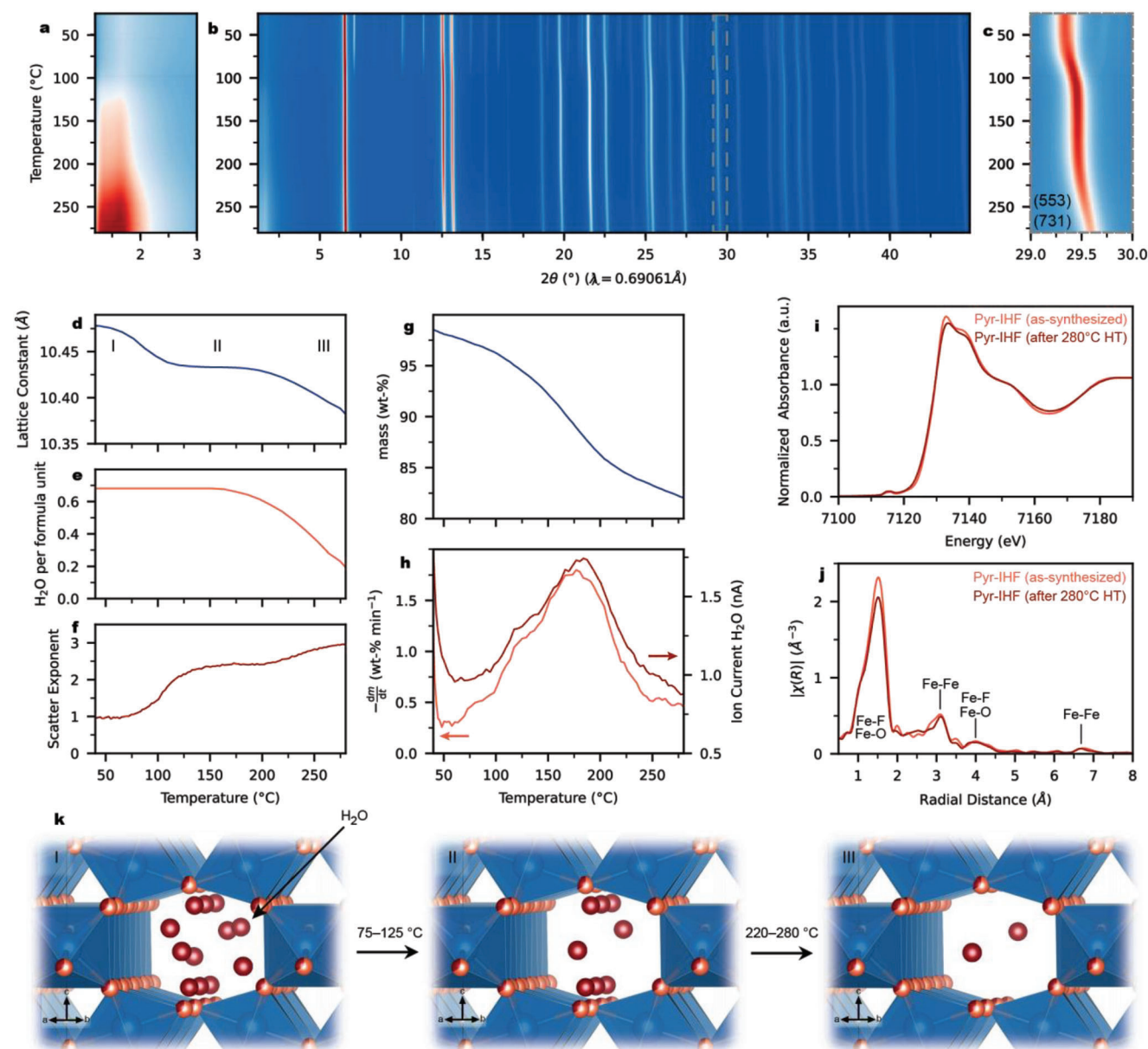
Figure 2. Structural Changes in Pyrochlore Iron Hydroxy Fluoride (Pyr-IHF) During Heat-treatment. a–c) Operando synchrotron XRD of the heat-treatment of as-synthesized Pyr-IHF. XRD patterns were recorded every 5 s. The temperature evolution of SAXS (a) and wide angle scattering (b) regime are displayed. c) Temperature evolution of the (553)/(731) reflex intensity and position. d,e) Temperature evolution for selected Rietveld parameters during the operando synchrotron XRD. The consistently low global residuals ($R_{wp} > 6.3\%$, Figure S9, Supporting Information) indicate the goodness of fit. d) shows the Pyr-IHF lattice constant evolution and e) the crystalline water content inside the channels. f) Fitted scattering exponent obtained from SAXS. g,h) Thermogravimetric (g) and mass spectrometric (h) analyses of dried Pyr-IHF. g) shows the temperature evolution of the absolute mass loss. h) shows the temperature evolution of the differential mass loss and ion currents for $m/z = 18$ (H_2O). i,j) X-ray absorption spectra of dried Pyr-IHF before and after heat treatment. i) shows the normalized XANES region of both species and j) shows the k^2-weighted EXAFS spectra in real space. k) shows a schematic representation of the H_2O loss in Pyr-IHF during heat treatment.

Importantly, the appearance of a small-angle X-ray scattering (SAXS) signal (scattering vectors of 2 – 5 nm^{-1}) at ≈75 °C, and the associated increase in the scatter exponent obtained by fitting the SAXS signal on a log–log scale, indicated that the surface morphology of the Pyr-IHF particles changes significantly during the release of disordered H_2O within the channels (Figure 2a,f, Figures S9,S12, Supporting Information and Experimental Section for details). A further increase in temperature to 280 °C, resulting in the release of crystalline water at T > 220 °C, does not appear to induce significant further morphological changes in the Pyr-IHF particles, as the scatter exponent increased only slightly. These results were consistent with a porosity increase observed on TEM images of as-synthesized Pyr-IHF and Pyr-IHF, which were heat-treated up to the temperature of 220 °C at

**ADVANCED
SCIENCE NEWS**

www.advancedsciencenews.com

**ADVANCED
MATERIALS**

www.advmat.de

1 °C min^{-1} (Figure S13, Supporting Information). Additional TEM and High Angle Annular Dark Field (HAADF) STEM measurements of Pyr-IHF heat-treated to 280 °C also confirmed that a further increase of temperature does not lead to further morphological changes of Pyr-IHF particles (Figures S14,S15, Supporting Information).

Next, considering that the significantly decreased scale factor of Pyr-IHF indicated partial amorphization of Pyr-IHF during heat-treatment, we quantified the content of the amorphous phase of Pyr-IHF before and after heat-treatment. The amorphous and crystalline phase fractions were refined by Rietveld refinement of XRD patterns of as-synthesized and 280 °C-heat-treated Pyr-IHF powders, each mixed with a highly crystalline Si powder (Experimental Section for details). Pyr-IHF contains 77 and 61 wt% crystalline phases before and after heat-treatment (Figure S16, Note S4, and Table S2, Supporting Information). It should be noted, however, that the appearance of a relatively large fraction of non-crystalline phase does not necessarily imply amorphization but rather a reduction in the crystallite size of Pyr-IHF, which is below the detection limit of XRD. Pyr-IHF powders display crystalline domains of 2–5 nm as can be seen from High-Resolution TEM micrographs and their Fourier transform patterns (Figure S15f,g, Supporting Information). Considering the Pyr-IHF unit cell size of 1.0 nm, those domains are composed of only 2 – 5 unit cells. While the local structure and its 3D interconnected channels are likely preserved, such domains are not detectable by XRD due to the short coherent scattering length.

To confirm that the local environment of Pyr-IHF is preserved, XAS spectra of Pyr-IHF before and after heat-treatment were obtained (Figure 2h,i; Figure S5, Supporting Information). The X-ray absorption near edge spectra (XANES) display highly similar pre-edge features and edge-position and more importantly, the EXAFS regions are identical, even down to the third coordination sphere at $\approx$7 Å. Moreover, the EXAFS spectra for the two Pyr-IHF samples differed significantly from other Fe^{3+}-containing references (Figure S5c, Supporting Information), further confirming that other phases are not present in significant amounts. Interestingly, the edge energy for Pyr-IHF is slightly decreased compared to FeF_3. This is consistent with the partial substitution of F^- ligands with OH^- ligands obtained from wavelet transform analysis (vide supra).

2.3. Electrochemical Performance

To evaluate the potential of 280 °C-heat-treated Pyr-IHF (Pyr-IHF · 0.38 H_2O) as a cathode material for Li-ion batteries, a series of electrochemical measurements were performed. Cathodes were prepared by ball-milling of Pyr-IHF with carbon black (CB) and polyvinylidene difluoride (pVdF) binder in N-methylpyrrolidone (NMP) solvent. The prepared slurry was tape casted onto a carbon-coated Al foil as a current collector. The resulting tape was dried in air at 80 °C, followed by vacuum drying at 80 °C for $\approx$24 h.

The as-prepared cathodes preserved the pyrochlore phase, local structure, and morphology of Pyr-IHF in the cathodes under slurry preparation conditions as indicated by powder XRD, XAS, and TEM measurements (Figures S17–S21, Supporting Information). Since the heat-treatment at 280 °C of the Pyr-IHF active

material and the cathode preparation were performed in air, the structure of Pyr-IHF in the cathode contained residual H_2O of crystallization (0.38 H_2O per formula unit).

Considering the known issue of poor cycling stability of metal fluoride cathodes in most conventional carbonate-based Li-ion electrolytes,[28–30] as well as the recently reported advanced capacity retention of metal fluoride cathodes in ionic liquid electrolyte by our group,[28] we performed a series of initial experiments to select a suitable electrolyte (Figure 3a–c; Figures S22,S23, Supporting Information). Thus, the cycling stability of Pyr-IHF cathodes was tested using a conventional carbonate electrolyte (1 M $LiPF_6$ in ethylene carbonate (EC)/dimethyl carbonate (DMC)) and an ionic liquid electrolyte (1 M Lithium bis(fluorosulfonyl)imide (LiTFSI) in 1-butyl-1-methylpyrrolidinium bis(trifluoromethylsulfonyl)imide ($Pyr_{1,4}$TFSI)).

Figure 3a,b and Figure S23 (Supporting Information) show the voltage profiles and incremental capacity plots of Pyr-IHF containing cathodes between 2 – 4.2 V at a current density of 100 mA g^{-1} ($\approx$0.4 C) for both electrolytes. The total discharge capacity was 171 mA h g^{-1}. 142 mA h g^{-1} of capacity can be extracted upon recharging, which corresponds to an initial coulombic efficiency of 120.6%. An irreversible capacity loss during the first cycle has been observed previously.[14,15] From the second cycle onward, the coulombic efficiency was improved significantly to 102.3(5)% for the next 250 cycles. Voltage profiles for Pyr-IHF containing cathodes with ionic liquid electrolytes (Figure 3b) were similar to those measured with carbonate-based Li-ion electrolytes. The initial coulombic efficiency was 126.2%. In the following cycles, however, the difference between the two electrolytes was evident. Only 16% of the initial charge capacity of Pyr-IHF-containing cathodes measured in the carbonate-based electrolyte was retained after 250 cycles. On the contrary, cells with ionic liquid electrolytes showed superior capacity retention of Pyr-IHF cathodes of 73% after 250 cycles under identical conditions. The consistently good coulombic efficiencies of 99.7(3)% after the first cycle further demonstrates superior cycling stability in ionic liquid-based electrolytes. Having established the superior cycling stability and coulombic efficiency of Pyr-IHF in ionic liquids, we investigated the rate capability of Pyr-IHF cathodes at different current densities (Figure S24, Supporting Information). The discharge capacity drops by $\approx$50% between the 10th and 60th cycle when the current was increased from 25 to 1000 mA g^{-1}, indicating either insufficient electronic conductivity or charge transfer kinetics in the Pyr-IHF cathodes. When the current rate was reduced to 25 mA g^{-1}, most of the capacity was recovered (128 mA h g^{-1} for the 10th cycle vs 110 mA h g^{-1} for the 110th cycle).

We hypothesized that the poor rate capability might stem from insufficient electronic percolation in the Pyr-IHF cathodes. It is known that even small amounts of carbon nanotubes (CNTs) can drastically improve electronic percolation.[31] Thus, multi-walled CNTs (1 wt%) were added during slurry preparation. Full cells with and without CNT-containing cathodes were then cycled galvanostatically at moderate (100 mA g^{-1}) and high (1000 mA g^{-1}) current rates. While the discharge capacity of the first cycle is almost identical (162 mA h g^{-1} vs 163 mA h g^{-1}) at 100 mA g^{-1} (Figure S25, Supporting Information), the addition of CNTs significantly improved the initial discharge/charge
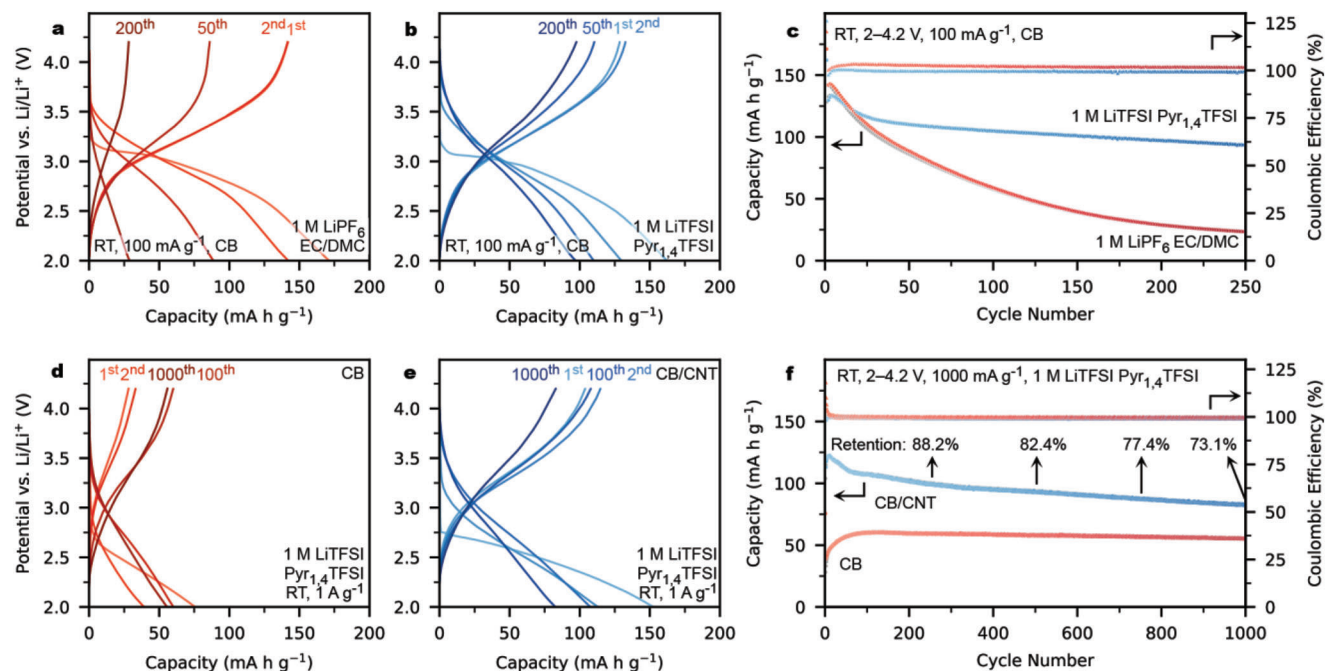
Figure 3. Electrochemical Performance of Pyrochlore Iron Hydroxy Fluoride (Pyr-IHF) Cathodes. a,b) Charge and discharge voltage profiles (2–4.2 V vs Li$^+$/Li) of full cells with Pyr-IHF cathodes and Li metal anodes in 1 M LiPF$_6$ in EC/DMC (a) and 1 M LiTFSI in Pyr$_{1,4}$TFSI (b) for selected cycles. c) Cycling stability of the cathodes shown in (a,b) (for magnification see Figure S22, Supporting Information). d,e) Charge and discharge voltage profiles (2–4.2 V vs Li$^+$/Li) for selected cycles of full cells with Pyr-IHF cathodes and Li metal anodes and 1 M LiTFSI in Pyr$_{1,4}$TFSI electrolyte. The cathode contained carbon black (CB) (d) and CB and 1 wt% of CNTs (e) as a conductive additive. f) Long-term cycling performance of the cathode shown in (d,e) (for magnification see Figure S25, Supporting Information).

capacity at 1000 mA g^{-1} (152/104 mA h g^{-1} vs 76/28 mA h g^{-1}) (Figure 3d,e) while maintaining very high coulombic efficiencies. Importantly, at higher current rates, the mean discharge and charge capacities over the subsequent 1000 cycles are significantly improved in the presence of CNTs (94/95 mA h g^{-1} vs 58/58 mA h g^{-1}). This indicates that electronic percolation was indeed a limiting factor at high current densities and can be mitigated by CNTs due to their high aspect ratio.[31] Notably, the cycling measurements of full cells using Pyr-IHF containing cathodes at the high current density of 1000 mA g^{-1} showed superior discharge capacity retention (excluding the capacity drop after the initial cycle) of 88.2%, 82.4%, 77.4%, and 73.4% after 250, 500, 750, and 1000 cycles, respectively (Figure 3f). To the best of our knowledge, this is one of the longest cycling performances demonstrated to date for iron (III) fluoride-based cathodes with a lower cutoff voltage of 2 V versus Li$^+$/Li (Figure S25g, Supporting Information).[11,14,32–45]

2.4. Impact of Water on the Electrochemical Performance

Next, to study the impact of the structural water on the electrochemical performance of Pyr-IHF, a series of cathodes consisting of Pyr-IHF with different water contents were prepared with CB as a conductive additive and cycled at moderate (100 mA g^{-1}) and high (1000 mA g^{-1}) current rates (**Figure 4**; Figures S26–S28, Supporting Information). The compositions of Pyr-IHF were as follows (see SI for synthesis details): i) Pyr-IHF · 0.53 H$_2$O,

ii) Pyr-IHF · 0.50 H$_2$O, iii) Pyr-IHF · 0.38 H$_2$O, and iv) Pyr-IHF · 0.21 H$_2$O.

The electrochemical performance of Pyr-IHF · 0.53 H$_2$O (i) and Pyr-IHF · 0.50 H$_2$O (ii) samples was found to be significantly different. Sample (i) was characterized by the lowest discharge capacities of 28 and 3 mA h g^{-1} at moderate and high current rates respectively, while sample (ii) demonstrated significantly higher values of 105 and 55 mA h g^{-1} at both rates (Table S3, Supporting Information). Since the crystalline H$_2$O content is almost identical between these two samples, but the surface morphology is significantly altered (Figure 4b; Figures S4,S13–S15,S29, Supporting Information), favorable morphology and reduced Li-ion diffusion pathways in the 220 °C-heat-treated Pyr-IHF (ii) may account for the significantly improved capacities. Importantly, samples (ii–iv), which have the same porosity, but differ only in H$_2$O content, also showed significant differences in the achievable capacities at both rates: 105/55 mA h g^{-1}, 162/75 mA h g^{-1} and 173/85 mA h g^{-1} for samples (ii), (iii) and (iii), respectively.

The fact that the highest capacities were measured for Pyr-IHF with the lowest content of water clearly demonstrates that both Li-ion storage and Li-ion diffusion are negatively affected by the presence of H$_2$O inside the channels. Hence, Li-ions must indeed diffuse through and intercalate into the channels of the pyrochlore structure, demonstrating its intercalation-type behavior. Notably, samples with high H$_2$O content (i–iii) display increased capacities over cycling. This can be explained by the exchange of H$_2$O molecules with Li-ions over time, further supporting the idea that Li-ions diffuse within the pyrochlore structure.

**ADVANCED
SCIENCE NEWS**

www.advancedsciencenews.com
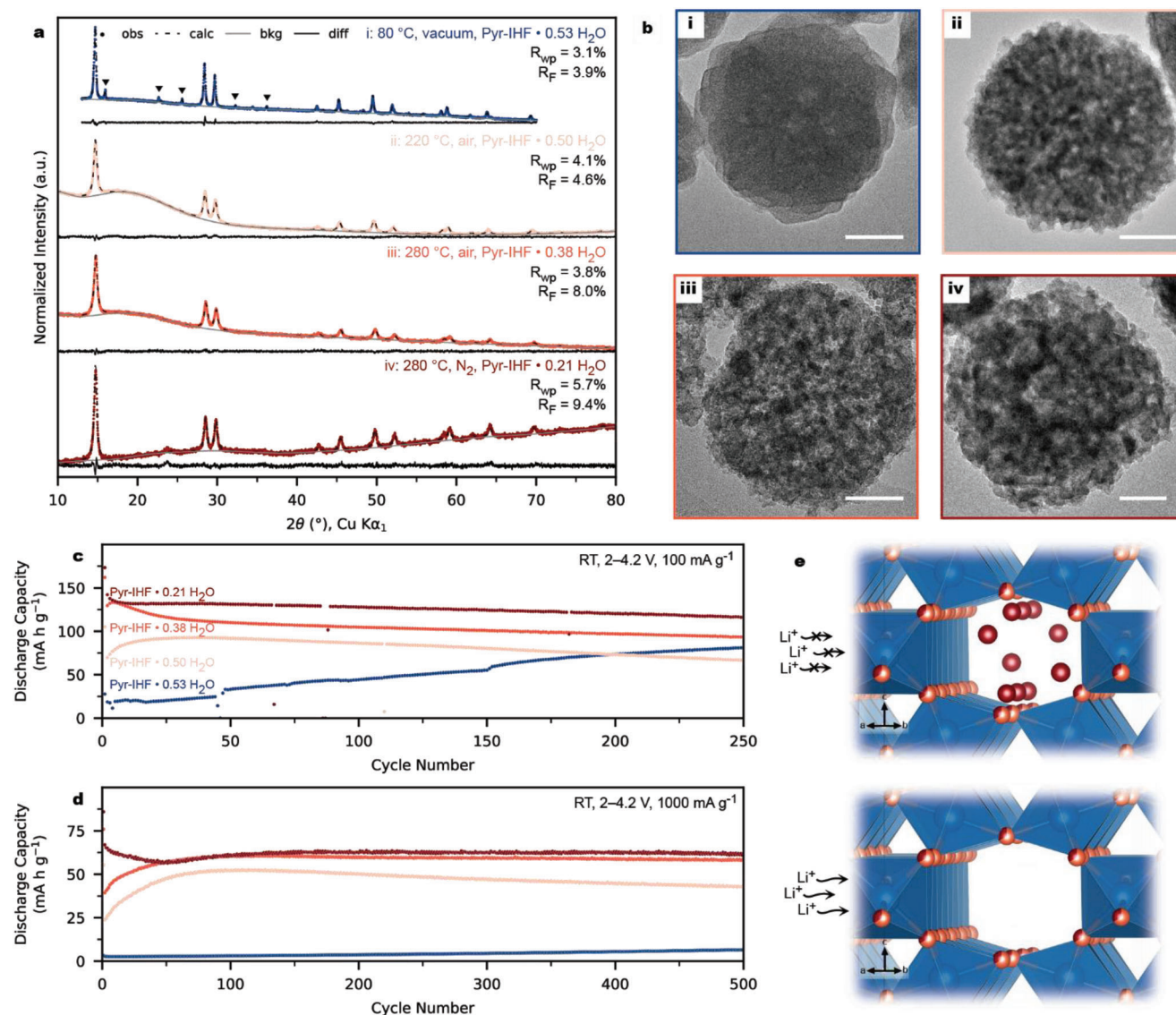
**ADVANCED
MATERIALS**

www.advmat.de

Figure 4. Influence of Morphology and Water of Crystallization on the Electrochemical Performance of Pyrochlore Iron Hydroxy Fluoride (Pyr-IHF) Cathodes. a) Rietveld refinements for the Pyr-IHF samples of different crystalline H_2O content (triangles indicate $FeF_3(H_2O)_2 \cdot H_2O$ impurities). b) High-resolution TEM micrographs (50 nm scale bars) of the same Pyr-IHF samples (dried under vacuum at 80 °C (i), heated to 220 °C under air (ii), heated to 280 °C under air (iii) and heated to 280 °C under N_2 (iv)). Further images and electron diffraction patterns are shown in Figures S4,S13–S15,S29 (Supporting Information). c,d) Cycling stability of full cells with Li metal anodes and the same Pyr-IHF cathodes in 1 M LiTFSI in $Pyr_{1,4}TFSI$ cycled between 2–4 V versus Li^+/Li at 100 mA g^{-1} (c) and 1000 mA g^{-1} (d). Circles indicate capacity and triangles indicate coulombic efficiency. Selected voltage profiles are shown in Figures S26–S28 (Supporting Information). e) Schematic representation of the effect of H_2O inside the channels of Pyr-IHF on the Li-ion storage ability.

3. Conclusion

In summary, we report a low-cost, highly scalable, and 100% atom-economical synthesis of Pyr-IHF with well-defined morphology and narrow particle size distribution. The facile dissolution–precipitation process effectively increases the dimensionality of Li-ion conducting channels (from 1D to 3D) while transitioning from the tetragonal $FeF_3(H_2O)_2 \cdot H_2O$ precursor to the cubic Pyr-IHF product. Heat-treatment of as-synthesized Pyr-IHF could selectively modify the morphology and solvent content within the 3D channels. Operando

SXRD measurements during heat-treatment demonstrated that changes in the surface morphology are linked – and likely caused by – the removal of disordered solvent molecules from the Pyr-IHF crystal structure. Without the need for a sophisticated synthesis or elaborate cathode designs, superior cycling stability of LIBs with heat-treated Pyr-IHF containing cathodes and IL electrolytes (>80% capacity retention after 600 cycles) at very high current rates (1 A g^{-1}, ≈4 C) demonstrates the potential of Pyr-IHF as a competitive low-cost cathode material. It should be noted, however, that given the significant costs associated with the use of CNT conductive additives and IL electrolytes,

**ADVANCED
SCIENCE NEWS**

www.advancedsciencenews.com

**ADVANCED
MATERIALS**

www.advmat.de

it is imperative that future research focus on identifying more economical alternatives. Finally, we used the modular synthesis via heat-treatment to selectively synthesize Pyr-IHF containing cathodes with different H_2O content. Removing water of crystallization from the channels significantly improves the capacity at moderate and high current densities. We rationalize this behavior by proposing that the channels inside the pyrochlore structure facilitate Li-ion diffusion, but only if the channels are not blocked with H_2O molecules. This work is the first demonstrated evidence for the Li-ion intercalation behavior in Pyr-IHF. Further investigations are currently being conducted to delve into the structural changes in Pyr-IHF during Li-ion intercalation.

4. Experimental Section

Synthesis of Pyr-IHF: $FeF_3(H_2O)_2$ · H_2O (1.0004(4) g, 5.9945(24) mmol, abcr chemicals, N_{sample} = 8, values denoted as mean value and standard deviation) was mixed with EtOH (150(10) mL, absolute for analysis, 99.8%, EMSURE, ACS) in a 250 mL capped bottle. The resulting suspension was stirred vigorously for 6 hours at room temperature to partially dissolve $FeF_3(H_2O)_2$·H_2O, forming an iron hydroxy fluoride ethanolic solution (1.03(7) g_{Fe} L_{EtOH}^{-1}), which was then centrifuged and filtered to separate it from the undissolved $FeF_3(H_2O)_2$ · H_2O (0.55(4) g, 3.28(22) mmol). The suspension was centrifuged (10 000 rpm, 5 min) and the clear yellow solution was decanted with a syringe. The solution was then filtered through a PTFE syringe filter (0.45 µm). Subsequently, 6.0(2) mL (4.0(3) vol-%) of distilled water was added to the solution and allowed to precipitate for 16 – 24 h. The suspension was then centrifuged (10 000 rpm, 5 min), and the collected beige powder of Pyr-IHF was dried under vacuum at 40 °C for 3 h for the SXRD experiment and subsequently dried under vacuum at 40 °C for at least 24 h for further use. The weight of the dried Pyr-IHF powder was (0.176(12) g, 1.47(10) mmol, 55(8)% yield based on the dissolved precursor). Identical yields (Pyr-IHF yield of 0.176(7) g, 1.47(6) mmol, 64(8)%) could be obtained by following the same procedure with a smaller amount of $FeF_3(H_2O)_2$ · H_2O (0.500(10) g, 3.00(6) mmol, N_{sample} = 5; ethanolic solution with 0.87(9) g_{Fe} L_{EtOH}^{-1}). This resulted in less undissolved $FeF_3(H_2O)_2$ · H_2O and increased the overall yield.

The amount of water added played an important role. Adding only 1.0 mL H_2O (1.5 vol-%) resulted in no precipitation. The addition of 2.0 mL H_2O (3 vol-%) resulted in significantly less Pyr-IHF product (0.092 g, 0.77 mmol, 31%).

Iron concentrations and therefore overall yields could be increased by dissolving $FeF_3(H_2O)_2$ · H_2O at 40 °C (1.7 g_{Fe} L_{EtOH}^{-1}). However, the resulting Pyr-IHF product (0.347 g, 2.89 mmol, 63%) contained a significant amount of $FeF_3(H_2O)_2$ · H_2O impurities after drying (Figure S30, Supporting Information).

Interestingly, the precipitation induced by simply evaporating the ethanolic iron fluoride solution at 80 °C resulted in the formation of the $FeF_3(H_2O)_2$ · H_2O with the tetragonal crystal structure (space group $P4/n$ (85)[17] Figure S31, Supporting Information). This suggested a crucial role of H_2O in the formation of the pyrochlore structure, most likely by condensating together the soluble precursors.

In addition to $FeF_3(H_2O)_2$ · H_2O, other suitable iron (III) fluoride-containing precursors were tested for solubility in ethanol and the formation of Pyr-IHF upon the addition of water. r-FeF_3 was poorly soluble in EtOH (≈0.6 g_{Fe} L_{EtOH}^{-1}) and no precipitate formed upon the addition of H_2O. Therefore, it was hypothesized that partially substituting the FeF_6 octahedra with more soluble anionic ligands like H_2O could increase the solubility. Hence, $FeF_3(H_2O)_2$ · H_2O with an average coordination sphere of $FeF_4(H_2O)_2$ was investigated and showed significantly improved solubility (≈1 g_{Fe} L_{EtOH}^{-1}). Encouraged by those results, that the solubility might be increased even further in the presence of a weakly-coordinating anion, iron (III) fluoride trifluoroacetate ($FeF_2(CF_3COO)$) with an average coor-

dination sphere of $FeF_4(CF_3COO)_2$ was therefore synthesized, displaying very high solubility (≈8 g_{Fe} L_{EtOH}^{-1}). Since the authors were interested in a cost-effective synthesis, $FeF_3(H_2O)_2$ · H_2O was chosen as the precursor for subsequent studies.

Synthesis of $FeF_2(CF_3COO)$: $FeF_2(CF_3COO)$ was synthesized according to a previous report by this group.[46]

Heat-Treatment of Pyr-IHF: As-synthesized Pyr-IHF (≈100 mg) was placed in a 2 mL glass vial in a tube furnace (Carbolite Gero) and the sides were sealed with quartz wool. Pyr-IHF was heated to 220 °C or 280 °C respectively for 30 min in air at heating rates of 1 and 10 °C min^{-1}, respectively, followed by a natural cooling rate by switching off the oven, resulting in the formation of Pyr-IHF containing 0.5 and 0.38 water of crystallization. Pyr-IHF·0.21H_2O was obtained by placing the Pyr-IHF-containing vial in a silica quartz tube that was fused on one side and opened on the other. The open tube end was then connected to a constant flow of N_2 by a valve and transferred into the tube furnace. As-synthesized Pyr-IHF was heated at 280 °C for 30 min at a heating rate of 10 °C min^{-1} and a natural cooling rate. The heat-treated Pyr-IHF sample was then stored in an Ar-filled glove box (GB) for further use. All heat-treated Pyr-IHF powders were orange-brown in color. It should be noted that longer residence times of 12 h at 280 °C or heat-treatment at temperatures > 350 °C resulted in the decomposition of Pyr-IHF. (Figure S32, Supporting Information).

Powder X-ray Diffraction Measurements: Powder XRD patterns were collected at RT on a Stoe STADI P powder X-ray diffractometer (Cu Kα1 radiation, λ = 1.540598 Å, focusing germanium monochromator) equipped with a Dectris Mythen 1 K silicon strip detector. Samples were normally prepared as thin powder films between two scotch tapes, placed in a transmission sample holder, and measured in Debye–Scherrer geometry. Pyr-IHF heated to 280 °C under N_2 was measured in a sealed 0.5 mm Ø borosilicate glass capillary to prevent contact with air. It was noted that the background signal for Pyr-IHF measured in the capillary was different from the samples measured between scotch tape due to the different absorption of the capillary compared to the scotch tape (Figure 5a).

Synchrotron Powder X-Ray Diffraction Measurements: SXRD data were obtained at the BM01 beamline at the European Synchrotron Radiation Facility. The X-ray beam (λ = 0.69061 Å) was monochromized with a double-crystal pair of flat Si(111) crystals and focused with two Rh-coated Si mirrors to a final beam size of ≈0.5 mm x 0.5 mm. Diffraction patterns were collected in transmission mode on a Pilatus 2 M area pixel-counting detector. Patterns were acquired for 60 sec. at RT under air. Pyr-IHF powder samples were loaded into borosilicate glass capillaries for measurement. As-prepared Pyr-IHF-containing cathodes were directly measured while cycled cathodes were dried from the electrolyte and then measured.

For the variable-temperature PXRD studies, the sample was heated under air to 280 °C at 12 K min^{-1} and cooled down again at 12 K min^{-1} using a Cryostream 700+. Data was acquired for 5 sec per shot (1 shot per °C) in a 2θ range of 2 – 45° with a step size of 0.0135°.

The SAXS signals were analyzed based on the operando SXRD experiment. To obtain the scatter exponent α, according to $I(q) = Sq^{-\alpha}$, a linear regression was performed on the natural logarithm of the signal intensity $I(q)$ against the natural logarithm of the scattering vector $q = \frac{4\pi}{\lambda} \sin(\theta)$ in the range of 2.7 nm^{-1} < q < 3.2 nm^{-1}. Smaller scattering vectors could not be used because of the beam stop and higher values deviated significantly from linearity (Figure S12, Supporting Information).

Rietveld Refinement: For the SXRD data, instrumental parameters were determined with a LaB$_6$ NIST standard. Rietveld refinement was performed with the GSAS-II program.[47] The background was modeled by a Chebyschev polynomial with 20 coefficients. The refined values for as-synthesized Pyr-IHF are summarized in Table S1 (Supporting Information).

For sequential Rietveld refinement, the Pyr-IHF models from the previous Rietveld refinement were used. Every fifth acquired pattern from the operando heat treatment of as-synthesized Pyr-IHF was refined (56 in total). The background was again modeled by a Chebyschev polynomial with 20 coefficients. Crystallite size, microstrain, and lattice parameters of Pyr-IHF with and without crystal water as well as the phase fraction of Pyr-IHF with and without crystal water were varied. Elastic strain relative

ADVANCED
SCIENCE NEWS

www.advancedsciencenews.com

ADVANCED
MATERIALS

www.advmat.de

to the initial lattice parameters was used to model the lattice parameters. All other parameters for the two Pyr-IHF phases were kept constant during sequential refinement (No. parameters: 26). In particular, the O content on the 16d site was fixed as well because initial refinements of the occupancy at the 16d site of representative patterns of as-synthesized Pyr-IHF, Pyr-IHF at 280 °C and Pyr-IHF after cooldown did not vary significantly.

For lab-scale powder XRD, a Si 640c NIST internal standard was mixed with different Pyr-IHF samples to determine instrumental parameters as well as non-crystalline and crystalline weight fractions (Note S4, Supporting Information). Since Cu-radiation was used, a significant fluorescence background was observed. This artificially improved the R-values from Rietveld refinement. Hence, prior to refinement, the constant background was reduced to 2% of the 111 reflection intensity to obtain reliable Figures of merit. The background was modeled by a Chebyschev polynomial with 20 coefficients. The Figures of merit for the refinements as well as the determined content of crystalline material are given in Table S2 (Supporting Information). The calculations used to determine the crystalline content are detailed in the Supporting Information.

Synchrotron X-Ray Absorption Spectroscopic Measurements: X-ray absorption data was obtained at the BM31 beamline at the European Synchrotron Radiation Facility. The X-ray beam was monochromatized using a liquid nitrogen double-crystal monochromator equipped with a pair of flat Si(111) crystals. Spectra were recorded in transmission mode at the Fe K-edge. For reference samples of different iron-containing compounds (Fe, FeF_2, Fe_2O_3, FeF_3, $FeF_3(H_2O)_2 \cdot H_2O$, $FeF_3 \cdot 0.33 H_2O$, as-synthesized Pyr-IHF, heat-treated Pyr-IHF to 280 °C under air), spectra were acquired at RT between $7.0 - 8.0$ keV, scanning continuously with ≈ 4 eV s^{-1}, with 3 repeats and a final beam size of ≈ 6 mm x 5 mm. Reference samples were prepared by grinding ≈ 12 mg of material with ≈ 88 mg of cellulose in a mortar for 5 min. The exact amount was chosen to obtain an edge step of 1.0. The powder was then pressed into 20 mm pellets with a pressing dye. For air-sensitive samples (FeF_2 and FeF_3), preparation was done in an Ar-filled GB and the pellet was sealed air-tight in a sealing bag. The samples were then stuck onto Kapton tape and mounted onto a sample holder. For the pristine Pyr-IHF-containing cathodes, the 12 mm cathode was folded onto itself multiple times before measurement to maximize signal intensity.

The wavelet transform of the experimental k^2-weighted EXAFS spectra between $3 - 14$ Å^{-1} was performed using the Matlab code of Muñoz et al.[48] Cauchy wavelets were used to back-transform the signal between $1 - 2$ Å.

Thermogravimetric Analysis with Evolved Gas Analysis: As-synthesized Pyr-IHF (5-10 mg) after vacuum drying at 40 °C for 24 h was placed in an Al crucible and transferred into the TGA. TGA and DSC were performed using a Netzsch Simultaneous Thermal Analyzer (STA 449 F5 Jupiter). The accuracy of the TGA was 0.1 µg. The sample was heated under Ar: O$_2$ flow (80:20 v:v, 40 mL min^{-1}) from 50 °C to 280 °C at 12 K min^{-1} and cooled down again at 12 K min^{-1}.

The evolved gases were detected with Netzsch Quadrupole mass spectrometer 403 D Aëolos Quadro using cross-beam electron impact ionization.

Fourier-Transform Infrared (FTIR) Spectroscopic Measurements: Attenuated total reflectance (ATR) FTIR spectra were recorded on a Thermo Scientific Nicolet iS5 FTIR spectrometer between 400 cm^{-1} and 4000 cm^{-1} with a resolution of 2 cm^{-1}.

(Scanning) Transmission Electron Microscopy ((S)TEM) Measurements: (S)TEM measurements were performed on a Talos F200X (ThermoFisher Scientific, FEG, U$_{acc}$ = 200 kV). Samples were prepared by dispersing Pyr-IHF in ethanol and depositing a few drops of the suspension onto a perforated carbon foil supported on a copper grid. Energy-dispersive X-ray spectroscopy (EDXS) was measured with four SDD detectors (Super-X EDS system) attached to the microscope column.

Battery Components: Carbon black (CB, Super C65, provided by TIMCAL), a glass–microfiber separator (Whatman), Poly(vinylidene fluoride) (pVdF, average Mw ≈ 534 g mol^{-1}, Sigma Aldrich), and *N*-Methyl-2-pyrrolidone (NMP, 99%, Sigma Aldrich), 1 M LiPF$_6$ in ethylene carbonate/dimethyl carbonate (1:1 v/v) (LP30, 99.9%, Solvionic), Lithium bis(trifluoromethanesulfonyl)imide (LiTFSI, 99+%, Solvionic), 1-Butyl-1-methylpyrrolidinium bis(trifluoromethylsulfonyl)imide (Pyr$_{1,4}$TFSI, 99%, iolitec, dried over molecular sieves prior to use), carbon nanotubes stabilized in NMP (Tuball Batt NMP 0.2%).

Fabrication of Batteries: In a typical cathode preparation, a slurry was prepared from Pyr-IHF (100 mg, 50 wt%), CB (80 mg, 40 wt%) and a solution of 0.833 wt% pVdF binder in NMP (20 mg, 10 wt% pVdF; 2400 mg, 1200 wt% NMP). The slurry was mixed under air in a ZrO$_2$ beaker (12 mL) with ZrO$_2$ balls (20 g, 5 mm Ø) and ball-milled in a planetary ball-mill (Fritsch, Pulverisette 7) for 1 h at 300 rpm. It was noteworthy that higher ball-milling rates of ≥ 500 rpm destroyed the Pyr-IHF crystal structure (Figure S17, Supporting Information). Similarly, an additional dry ball-milling step at 300 rpm to mix Pyr-IHF with CB prior to wet grinding in NMP amorphized the Pyr-IHF structure completely (Figure S17, Supporting Information). Therefore, higher ball-milling speeds or additional dry-ball-milling steps were not used for slurry preparation.

The slurry was then immediately tape-casted onto carbon-coated Al foil with a doctor blade of 100 µm at a speed of 1 mm s^{-1} to obtain a uniform tape (≈ 6 cm x 30 cm). The tape-casted Al foil was dried under air at 80 °C until visibly dry (≈ 3 h) and then dried under vacuum at 80 °C for at least 20 h. Disks (12 mm Ø) were punched out of the foil, weighed (mean active material loadings with standard deviation was 0.46(14) mg cm^{-2}) and transferred into an Ar-filled GB. In an Ar-filled glovebox, the cathode was wetted with 150 µL of the Li-ion conducting electrolyte (LP30 or 1 M LiTFSI in Pyr$_{1,4}$TFSI). IL-wetted cathodes were then heated under Ar for 24 h at 70 °C to ensure good wetting of the cathode. The cathode was then incorporated with a glass microfiber separator into an air-tight stainless-steel coin-type cell (CR2032, 316L, Hohsen Corp). Elemental Li coins (12 mm Ø) were used as counter and reference electrodes.

For initial experiments, Pyr-IHF with 0.38 H$_2$O per formula unit of water of crystallization was used. For optimized cathodes, a pVdF / NMP solution with stabilized CNTs (0.2 wt% CNT, 2 wt% pVdF) was used. The slurry recipe was the same but with a conductive additive mixture of 1 wt% CNT and 39 wt% CB.

For the cathode used in operando XAS measurements, the same procedure was followed but the cathode slurry was tape-casted with a doctor blade of 200 µm. The tape was dried at 80 °C and a subsequent tape-casting with a doctor blade of 200 µm was performed. The cell was then dried as described above.

For the investigation of the influence of water on the electrochemical performance, Pyr-IHF active materials with different H$_2$O content were prepared. The following conditions were chosen to obtain different water contents. i) Sample (as-synthesized Pyr-IHF·0.53 H$_2$O) was dried under vacuum at 80 °C to remove surface-adsorbed water and ethanol molecules. XRD and TEM analysis (Figure 4a,b; Figure S4, Supporting Information) confirmed that the morphology and structure of the material remained preserved during the vacuum drying process. ii) Sample (Pyr-IHF·0.50 H$_2$O) was prepared by heat-treating the as-synthesized Pyr-IHF to 220 °C at a heating rate of 1 °C min^{-1} in air. The temperature of 220 °C was chosen as it allows for morphological changes while still retaining crystalline water within the channels (Figure 2; Figure S13, Supporting Information). TEM and XRD analysis (Figure 2; Figure S13, Supporting Information) demonstrated that the heating rate (ranging from 1 to 10 °C min^{-1} with a 30-minute dwell time) had negligible influence on the morphology and structural water content. iii) Sample (Pyr-IHF·0.38 H$_2$O) was prepared by heat-treating the as-synthesized Pyr-IHF to 280 °C in air. The electrode containing samples (i), (ii), and (iii) were all prepared under air using the procedures described earlier. iv) Sample (Pyr-IHF·0.21 H$_2$O) was prepared using the same heat-treatment conditions as sample (iii), but under a nitrogen atmosphere to prevent partial rehydration during the cooling process (Figure S9b, Supporting Information). The entire slurry preparation for electrodes containing sample (iv) was conducted under an inert atmosphere.

Inside an Ar-filled GB, the slurry was mixed in the ZrO$_2$ beaker as described above. The beaker was then wrapped in two medical protection covers and sealed. The slurry was then transferred out of the GB and ball-milled with the same program as mentioned above. Afterward, the sample

2304158 (9 of 11)

was transferred back into the GB and the slurry was manually tape-cast onto Al-foil with a doctor blade of 100 μm. The tape was dried at 80 °C for 2 h before drying it in a GB antechamber under.

Electrochemical Measurements: Galvanostatic cycling was performed in a voltage range between 2 – 4.2 V on a multichannel potentiostat/ galvanostat from Biologic (MPG2) or Astrol BAT-Flex. All cells were measured at 25 – 28 °C. C-rates were calculated assuming a 1 e^- reduction of Fe (III) to Fe (II) (237 mA h g^{-1}).

Supporting Information

Supporting Information is available from the Wiley Online Library or from the author.

Acknowledgements

Conflict of Interest

The authors declare no conflict of interest.

Data Availability Statement

The data that support the findings of this study are available from the corresponding author upon reasonable request.

Keywords

[1] D. Larcher, J.-M. Tarascon, *Nat. Chem.* **2015**, *7*, 19.
[2] T. Liu, Y. Zhang, Z. Jiang, X. Zeng, J. Ji, Z. Li, X. Gao, M. Sun, Z. Lin, M. Ling, J. Zheng, C. Liang, *Energy Environ. Sci.* **2019**, *12*, 1512.
[3] K. Turcheniuk, D. Bondarev, V. Singhal, G. Yushin, *Nature* **2018**, *559*, 467.
[4] E. Fan, L. Li, Z. Wang, J. Lin, Y. Huang, Y. Yao, R. Chen, F. Wu, *Chem. Rev.* **2020**, *120*, 7020.
[5] M. Walter, M. V. Kovalenko, K. V. Kravchyk, *New J. Chem.* **2020**, *44*, 1677.
[6] K. V. Kravchyk, T. Zünd, M. Wörle, M. V. Kovalenko, M. I. Bodnarchuk, *Chem. Mater.* **2018**, *30*, 1825.
[7] G. G. Amatucci, N. Pereira, *J. Fluorine Chem.* **2007**, *128*, 243.
[8] F. Badway, N. Pereira, F. Cosandey, G. G. Amatucci, *J. Electrochem. Soc.* **2003**, *150*, A1209.
[9] X. Hua, A. S. Eggeman, E. Castillo-Martínez, R. Robert, H. S. Geddes, Z. Lu, C. J. Pickard, W. Meng, K. M. Wiaderek, N. Pereira, G. G. Amatucci, P. A. Midgley, K. W. Chapman, U. Steiner, A. L. Goodwin, C. P. Grey, *Nat. Mater.* **2021**, *20*, 841.
[10] Q. Huang, K. Turcheniuk, X. Ren, A. Magasinski, A.-Y. Song, Y. Xiao, D. Kim, G. Yushin, *Nat. Mater.* **2019**, *18*, 1343.
[11] F. Wu, V. Srot, S. Chen, S. Lorger, P. A. van Aken, J. Maier, Y. Yu, *Adv. Mater.* **2019**, *31*, 1905146.
[12] K. Lemoine, A. Hémon-Ribaud, M. Leblanc, J. Lhoste, J.-M. Tarascon, V. Maisonneuve, *Chem. Rev.* **2022**, *122*, 14405.
[13] L. Sun, Y. Li, W. Feng, *Small Methods* **2023**, *7*, 2201152.
[14] C. Li, C. Yin, L. Gu, R. E. Dinnebier, X. Mu, P. A. van Aken, J. Maier, *J. Am. Chem. Soc.* **2013**, *135*, 11425.
[15] K. Lemoine, L. Zhang, D. Dambournet, J.-M. Grenèche, A. Hémon-Ribaud, M. Leblanc, O. J. Borkiewicz, J.-M. Tarascon, V. Maisonneuve, J. Lhoste, *Chem. Mater.* **2019**, *31*, 4246.
[16] M. A. Hepworth, K. H. Jack, R. D. Peacock, G. J. Westland, *Acta Cryst.* **1957**, *10*, 63.
[17] G. Teufer, *Acta Cryst.* **1964**, *17*, 1480.
[18] M. Leblanc, G. Ferey, P. Chevallier, Y. Calage, R. de Pape, *J. Solid State Chem.* **1983**, *47*, 53.
[19] H. J. Tan, H. L. Smith, L. Kim, T. K. Harding, S. C. Jones, B. Fultz, *J. Electrochem. Soc.* **2014**, *161*, A445.
[20] R. de Pape, G. Ferey, *Mater. Res. Bull.* **1986**, *21*, 971.
[21] C. Li, L. Gu, S. Tsukimoto, P. A. van Aken, J. Maier, *Adv. Mater.* **2010**, *22*, 3650.
[22] N. Stock, S. Biswas, *Chem. Rev.* **2012**, *112*, 933.
[23] C. S. Cundy, P. A. Cox, *Chem. Rev.* **2003**, *103*, 663.
[24] J. Nai, X. W. D. Lou, *Adv. Mater.* **2019**, *31*, 1706825.
[25] H. Funke, A. C. Scheinost, M. Chukalina, *Phys. Rev. B* **2005**, *71*, 94110.
[26] M. Burbano, M. Duttine, O. Borkiewicz, A. Wattiaux, A. Demourgues, M. Salanne, H. Groult, D. Dambournet, *Inorg. Chem.* **2015**, *54*, 9619.
[27] M. Duttine, D. Dambournet, N. Penin, D. Carlier, L. Bourgeois, A. Wattiaux, K. W. Chapman, P. J. Chupas, H. Groult, E. Durand, A. Demourgues, *Chem. Mater.* **2014**, *26*, 4190.
[28] J. F. Baumgärtner, F. Krumeich, M. Wörle, K. V. Kravchyk, M. V. Kovalenko, *Commun. Chem.* **2022**, *5*, 6.
[29] F. Wu, G. Yushin, *Energy Environ. Sci.* **2017**, *10*, 435.
[30] A. J. Gmitter, F. Badway, S. Rangan, R. A. Bartynski, A. Halajko, N. Pereira, G. G. Amatucci, *J. Mater. Chem.* **2010**, *20*, 4149.
[31] X. Zeng, X. Xu, P. M. Shenai, E. Kovalev, C. Baudot, N. Mathews, Y. Zhao, *J. Phys. Chem. C* **2011**, *115*, 21685.
[32] D. Ma, Z. Cao, H. Wang, X. Huang, L. Wang, X. Zhang, *Energy Environ. Sci.* **2012**, *5*, 8538.
[33] C. Li, X. Mu, P. A. van Aken, J. Maier, *Adv. Energy Mater.* **2013**, *3*, 113.
[34] C. Li, C. Yin, X. Mu, J. Maier, *Chem. Mater.* **2013**, *25*, 962.
[35] J. Liu, Y. Wan, W. Liu, Z. Ma, S. Ji, J. Wang, Y. Zhou, P. Hodgson, Y. Li, *J. Mater. Chem. A* **2013**, *1*, 1969.
[36] Y.-L. Shi, N. Wu, M.-F. Shen, Y.-L. Cui, L. Jiang, Y.-H. Qiang, Q.-C. Zhuang, *ChemElectroChem* **2014**, *1*, 645.
[37] C. P. Guntlin, T. Zünd, K. V. Kravchyk, M. Wörle, M. I. Bodnarchuk, M. V. Kovalenko, *J. Mater. Chem. A* **2017**, *5*, 7383.
[38] L.-P. Wang, T.-S. Wang, X.-D. Zhang, J.-Y. Liang, L. Jiang, Y.-X. Yin, Y.-G. Guo, C.-R. Wang, *J. Mater. Chem. A* **2017**, *5*, 18464.
[39] Y. Bai, X. Zhou, C. Zhan, L. Ma, Y. Yuan, C. Wu, M. Chen, G. Chen, Q. Ni, F. Wu, R. Shahbazian-Yassar, T. Wu, J. Lu, K. Amine, *Nano Energy* **2017**, *32*, 10.
[40] E. Zhao, O. Borodin, X. Gao, D. Lei, Y. Xiao, X. Ren, W. Fu, A. Magasinski, K. Turcheniuk, G. Yushin, *Adv. Energy Mater.* **2018**, *8*, 1800721.

[41] S. Tawa, Y. Sato, Y. Orikasa, K. Matsumoto, R. Hagiwara, *J. Power Sources* **2019**, *412*, 180.

[42] G. Chen, X. Zhou, Y. Bai, Y. Yuan, Y. Li, M. Chen, L. Ma, G. Tan, J. Hu, Z. Wang, F. Wu, C. Wu, J. Lu, *Nano Energy* **2019**, *56*, 884.

[43] L. Zhang, L. Yu, O. L. Li, S.-Y. Choi, G. Saeed, K. H. Kim, *J. Mater. Chem. A* **2021**, *9*, 16370.

[44] J. Ding, X. Zhou, C. Luo, J. Yang, J. Tang, *New J. Chem.* **2021**, *45*, 18019.

[45] J. Ding, X. Zhou, C. Luo, H. Xu, J. Yang, J. Tang, *J. Mater. Sci.* **2022**, *57*, 1261.

[46] M. Wörle, C. P. Guntlin, L. Gyr, M. T. Sougrati, C.-H. Lambert, K. V. Kravchyk, R. Zenobi, M. V. Kovalenko, *Chem. Mater.* **2020**, *32*, 2482.

[47] B. H. Toby, R. B. von Dreele, *J. Appl. Cryst.* **2013**, *46*, 544.

[48] M. Muñoz, F. Farges, P. Argoul, *Phys. Scr.* **2005**, *115*, 221.